Supplementary Materials

CONTENTS

S1. Theoretical description 5
  S1.1. Narrow Feshbach resonance model for Li-K mixtures 5
  S1.2. Truncated Basis Method 6
  S1.3. Functional Determinant Approach 7

S2. Role of physical processes on different time scales 8
  S2.1. Multiple particle-hole excitations 8
  S2.2. Impurity mass 9
  S2.3. Temperature 10

S3. Role of interaction during finite-length rf pulses 11
  S3.1. Idealized versus realized Ramsey scenario 11
  S3.2. Modelling of rf pulses within TBM 12
  S3.3. Modelling of experimental procedure at finite temperature within FDA 13
  S3.4. Stronger interactions during rf pulses: illustration of quantum state preparation 14

S4. Universal features of impurity dynamics and relation to orthogonality catastrophe 15

S5. Experimental and data analysis procedures 16
  S5.1. Sample preparation 16
  S5.2. Rf pulses 18
  S5.3. Analysis methods 18
  S5.4. Varying the K concentration 18

S6. Linearity of rf response 19

References 20

S1. THEORETICAL DESCRIPTION

In this section, we summarize the approaches that we developed to theoretically model the results of our interferometric Ramsey experiments. We first discuss the microscopic model that we use to describe the narrow Feshbach resonance of the Li-K mixture, and then we outline how we calculate the time evolution of the system within two approaches: the Truncated Basis Method (TBM) and the Functional Determinant Approach (FDA). In this section, we assume that a 'perfect quench' is performed, where the impurity is initially non-interacting with the Fermi sea and there are no interactions during the radio-frequency (rf) pulses. A discussion of the role played by interactions during the rf pulses is deferred to Section S3.

S1.1. Narrow Feshbach resonance model for Li-K mixtures

In our experiment, the K impurities are concentrated in the central region of the Li Fermi gas where they experience a nearly uniform Li environment (see Section S5.A). Hence we consider in our model K impurities that are immersed in a Li Fermi gas of uniform density. The Li-K mixture is prepared at magnetic fields near a closed-channel dominated Feshbach resonance between the Li$|1\rangle$ and K$|3\rangle$ states that occurs near 155 G. The narrow character of this resonance is a consequence of the limited strength of the coupling of atoms in the open channel to a closed-channel molecular state. To describe this system we use the two-channel Hamiltonian

$$\begin{aligned}\hat{H} = &\sum_{\mathbf{k}} \epsilon_{\mathbf{k},\mathrm{Li}} \hat{c}^\dagger_{\mathbf{k}} \hat{c}_{\mathbf{k}} + \sum_{\mathbf{k}} \epsilon_{\mathbf{k},\mathrm{K}} \hat{d}^\dagger_{\mathbf{k}} \hat{d}_{\mathbf{k}} + \sum_{\mathbf{k}} \left[\epsilon_{\mathbf{k},M} + \epsilon_M(B)\right] \hat{b}^\dagger_{\mathbf{k}} \hat{b}_{\mathbf{k}} \\ &+ \frac{g}{\sqrt{V}} \sum_{\mathbf{k},\mathbf{q}} \chi(\mathbf{k}) \left(\hat{b}^\dagger_{\mathbf{q}} \hat{c}_{\mathbf{q}/2+\mathbf{k}} \hat{d}_{\mathbf{q}/2-\mathbf{k}} + \hat{d}^\dagger_{\mathbf{q}/2-\mathbf{k}} \hat{c}^\dagger_{\mathbf{q}/2+\mathbf{k}} \hat{b}_{\mathbf{q}} \right),\end{aligned} \tag{1}$$

where the first line defines the non-interacting Hamiltonian $\hat{H}_0$. Here, V is the total system volume, $\hat{c}^\dagger_{\mathbf{k}}$ ($\hat{c}_{\mathbf{k}}$) creates (annihilates) a Li fermion with momentum $\hbar\mathbf{k}$ and single-particle energy $\epsilon_{\mathbf{k},\mathrm{Li}} = \frac{\hbar^2 k^2}{2m_{\mathrm{Li}}}$, and $\hat{d}^\dagger_{\mathbf{k}}$ ($\hat{d}_{\mathbf{k}}$) creates (annihilates) a K impurity atom in the K$|3\rangle$ state with dispersion $\epsilon_{\mathbf{k},\mathrm{K}} = \frac{\hbar^2 k^2}{2m_{\mathrm{K}}}$, where we define $k \equiv |\mathbf{k}|$. The closed-channel molecule is created (annihilated) by $\hat{b}^\dagger_{\mathbf{k}}$ ($\hat{b}_{\mathbf{k}}$). It has the dispersion $\epsilon_{\mathbf{k},M} = \frac{\hbar^2 k^2}{2(m_{\mathrm{K}}+m_{\mathrm{Li}})}$, and a bare energy relative to the scattering threshold, $\epsilon_M(B) = \delta\mu(B - B_c)$. Here $\delta\mu$ is the differential magnetic moment between the open and closed channels, and B_c denotes the threshold crossing of the bare molecular state [27].

Close to the Feshbach resonance, the scattering length a diverges and the interaction between the K impurities and the Li atoms is predominantly mediated by exchange of the closed-channel molecule. We therefore neglect the background scattering potential in the open channel [14]. The strength of the coupling between the open and closed channels is given by g, and we take a form factor $\chi(\mathbf{k}) = 1/[1 + (r_0 k)^2]$, which accounts for the finite extent r_0 of the closed-channel wave function $\sim e^{-r/r_0}/r$.

The parameters of the model $\delta\mu$, B_c, g, and r_0 are fully determined by known experimental parameters. First, the differential magnetic moment has recently been measured to be $\delta\mu = h\times 2.35(2)$ MHz/G [12]. Second, close to resonance, the scattering length may be parametrized as

$$a = a_{\mathrm{bg}}\left(1 + \frac{\Delta B}{B_0 - B}\right) \approx a_{\mathrm{bg}}\frac{\Delta B}{B_0 - B}, \tag{2}$$

where B_0 is the center of the Feshbach resonance with width $\Delta B = 0.880\,\mathrm{G}$ and background scattering length $a_{\mathrm{bg}} = 63.0\,a_0$ [14]. To connect with our model, we consider the on-shell two-body scattering amplitude $f(k)$, which for the Hamiltonian (1) is given by [28]

$$f(k) = \frac{\mu_{\mathrm{red}} g^2 \chi(\mathbf{k})^2}{2\pi\hbar^2}\left[-\frac{\hbar^2 k^2}{2\mu_{\mathrm{red}}} + \epsilon_M(B) - \frac{g^2\mu_{\mathrm{red}}}{4\pi\hbar^2 r_0[1 - ikr_0]^2}\right]^{-1}, \tag{3}$$

where $\mu_{\mathrm{red}} = m_{\mathrm{Li}}m_{\mathrm{K}}/(m_{\mathrm{Li}} + m_{\mathrm{K}})$ is the reduced mass and $\mathbf{k}$ is the relative scattering wave vector. Using the low energy expansion $f^{-1}(k) \approx -a^{-1} + \frac{1}{2}r_{\mathrm{eff}}k^2 - ik$, with r_{eff} the effective range, we thus identify

$$a = \frac{1}{\frac{1}{2r_0} + 2R^*\mu_{\mathrm{red}}\delta\mu(B - B_c)/\hbar^2}, \tag{4}$$

$$r_{\mathrm{eff}} = -2R^* + 3r_0 - 4r_0^2/a, \tag{5}$$

where $R^* \equiv \hbar^4\pi/(\mu_{\mathrm{red}}^2 g^2)$ is the range parameter of the Feshbach resonance [29, 30]. Comparing Eqs. (2) and (4) yields

$$R^* = \frac{\hbar^2}{2\mu_{\mathrm{red}}a_{\mathrm{bg}}\delta\mu\Delta B}, \tag{6}$$

$$B_0 - B_c = \frac{1}{2}\Delta B a_{\mathrm{bg}}/r_0. \tag{7}$$

Equation (6) relates R^*, and thus the coupling constant g, to the known experimental parameters. The extent of the closed-channel wave function r_0 in turn follows by comparing Eq. (7) to the theoretical prediction from quantum defect theory [31, 32], $B_0 - B_c = a_{\mathrm{bg}}\Delta B/\bar{a}$, where $\bar{a} = 0.955 l_{\mathrm{vdw}}$ and $l_{\mathrm{vdw}} = 40.8\,a_0$ is the van der Waals length [14]. Thus we obtain $r_0 = \bar{a}/2$. Finally, B_0 was obtained in Ref. [12], allowing the determination of B_c.

S1.2. Truncated Basis Method

To model a mobile impurity as in the experiment, we consider an approximate wave function for the zero-momentum impurity that incorporates the scattering of a single particle out of the Fermi sea:

$$|\psi_{\boldsymbol{\alpha}}\rangle = \alpha_0 \hat{d}^\dagger_{\mathbf{0}}|\mathrm{FS}\rangle + \sum_{\mathbf{q}}\alpha_{\mathbf{q}}\hat{b}^\dagger_{\mathbf{q}}\hat{c}_{\mathbf{q}}|\mathrm{FS}\rangle + \sum_{\mathbf{k},\mathbf{q}}\alpha_{\mathbf{k},\mathbf{q}}\hat{d}^\dagger_{\mathbf{q}-\mathbf{k}}\hat{c}^\dagger_{\mathbf{k}}\hat{c}_{\mathbf{q}}|\mathrm{FS}\rangle\,. \tag{8}$$

Here, the first term on the right hand side describes the product state of the impurity K atom at zero momentum and the ground state of the non-interacting Li Fermi sea $|\mathrm{FS}\rangle = \prod_{|\mathbf{k}|<k_F}\hat{c}^\dagger_{\mathbf{k}}|0\rangle$, where k_F is the Fermi momentum, which is related to the Fermi energy by $\epsilon_F = \hbar^2 k_F^2/(2m_{\mathrm{Li}})$. The last two terms correspond, respectively, to the impurity

binding a Li atom to form a closed-channel molecule, and the impurity exciting a particle out of the Fermi sea, in both cases leaving a hole behind. When using the TBM, we focus on zero temperature in order to capture the purely quantum evolution of the impurity. For convenience, within this model we also take $r_0 \to 0$, which formally requires taking the bare crossing $B_c \to \infty$ to keep a finite. This approximation is justified, as R^* exceeds r_0 by about two orders of magnitude.

Truncated wave functions of the form (8) have been used extensively in the study of Fermi polarons in ultracold atomic gases, starting with the work of Chevy [18]. While most of the previous work has focused on equilibrium properties, recently it has been proposed that these wave functions may be extended to dynamical problems using a variational approach to obtain the equations of motion [33], for instance to calculate the decay rate of excited states.

Here, we adapt the use of truncated wave functions for the Fermi polaron to the calculation of the dynamical response of the impurity to an interaction quench. For a perfect quench and at zero temperature, the quantity measured in experiment corresponds to the overlap between the interacting and non-interacting states of the system, i.e., we have [10, 11]

$$S(t) = \langle \psi_0(t)|\psi_{\rm int}(t)\rangle = \langle \psi_0|\, e^{i\hat{H}_0 t/\hbar} e^{-i\hat{H}t/\hbar}\, |\psi_0\rangle \,. \tag{9}$$

Here $|\psi_0\rangle \equiv \hat{d}_{\mathbf{0}}^\dagger\,|{\rm FS}\rangle$ is the initial non-interacting state of energy E_0, and $\psi_{\rm int}(t)$ is the state after a quench at time $t = 0$ from zero to finite impurity interactions with the Fermi sea. Formally expanding in a complete set of states for the single impurity problem, the Ramsey signal (9) then becomes

$$S(t) = \sum_j |\langle \psi_0|\phi_j\rangle|^2\, e^{-i(E_j - E_0)t/\hbar}, \tag{10}$$

where $|\phi_j\rangle$ is an eigenstate of the interacting Hamiltonian with energy E_j. However, this requires one to solve the entire problem which is generally not possible for a mobile impurity. Thus, within the Truncated Basis Method (TBM), we restrict the Hilbert space to wave functions of the form (8) and diagonalize the Hamiltonian within this truncated basis. As we shall see, this truncation permits an extremely accurate description of the initial quantum dynamics of the impurity.

For small t, we expand $e^{-i\hat{H}t/\hbar}$ to find

$$S(t) \approx 1 - (t/\tau_F)^2 \frac{(1 + m_{\rm Li}/m_{\rm K})^2}{3\pi k_F R^*}, \tag{11}$$

with τ_F the Fermi time. This reveals that the short-time dephasing dynamics of $S(t)$ is completely determined by the two-body properties, which are captured exactly by the TBM. As we will see below, the TBM describes the impurity behavior also beyond the two-body timescale since higher order correlations and multiple particle-hole excitations take longer to build up. Indeed, for a mobile impurity and for sufficiently weak attraction where the attractive polaron is the ground state, the TBM correctly describes the long-time behavior $S(t) \to |\alpha_0|^2 e^{-i\varepsilon_p t/\hbar}$. Here, $|\alpha_0|^2$ is the polaron residue (squared overlap with the non-interacting state) and ε_p is the polaron energy, which are both accurately determined using a wave function of the form (8) [34].

With the TBM we consider zero temperature in order to isolate the quantum dynamics of the impurity. To better model the experiment, in principle one can extend the TBM to finite temperature by taking the initial state to be a statistical thermal distribution involving multiple impurity momenta. However, a more convenient approach at finite temperature is described in the next section.

S1.3. Functional Determinant Approach

At times t substantially exceeding τ_F, the full description of the impurity dynamics requires the inclusion of multiple particle-hole pair excitations as well as the effect of finite temperature, both of which present a theoretical challenge. In order to study and describe both effects, we employ the Functional Determinant Approach (FDA) [11, 35–37].

In the FDA the impurity is treated as an infinitely heavy object. In this limit, the FDA provides an exact solution of the dynamical many-body problem at arbitrary temperatures and times. The justification of the infinite mass approximation, which will be discussed in more detail in Section S2, is rooted in two observations. First, in our experiment, the mass of the K impurities is much larger than that of the Li atoms (mass ratio $m_{\rm K}/m_{\rm Li} \approx 6.7$) which constitute the surrounding Fermi gas. Therefore, the recoil energy gained by the K impurities due to the scattering with a Li atom is small. We estimate the typical recoil momentum k_R by averaging over all possible scattering processes on the Fermi surface, yielding $k_R = 4k_F/3$. From that we obtain an estimate for the typical recoil energy $E_R = \frac{16}{9}\frac{m_{\rm Li}}{m_{\rm K}}\epsilon_F \approx 0.25\epsilon_F$, which determines a typical time scale $\tau_R = \hbar/E_R \approx 4\tau_F$, up to which one expects recoil to have a minimal effect on the many-body quantum dynamics, cf. Section S2.2. Second, at times exceeding the thermal time scale $\tau_T = \hbar/(k_B T)$, which in our experiment is given by $\tau_T \approx 6\tau_F$, thermal effects due to the averaging over various statistical realizations become relevant. The resulting thermal fluctuations disrupt the coherent quantum propagation of the impurity, and hence, for times $t > \tau_T$, mask the effect of recoil [38].

To a good approximation, we may thus take the limit of infinite impurity mass, which admits the mapping of Eq. (1) onto the bilinear Hamiltonian

$$\hat{H} = \epsilon_M(B)\hat{m}^\dagger\hat{m} + \sum_{\mathbf{k}} \epsilon_{\mathbf{k}}\hat{c}^\dagger_{\mathbf{k}}\hat{c}_{\mathbf{k}} + g\sum_{\mathbf{k}}\chi(\mathbf{k})[\hat{m}^\dagger\hat{c}_{\mathbf{k}} + \hat{m}\hat{c}^\dagger_{\mathbf{k}}]. \tag{12}$$

Here, $\hat{m}^\dagger$ is the creation operator of the localized closed channel molecule and the interaction is described by the annihilation of a Li atom converting the empty impurity molecular state into an occupied one. By taking the limit $m_{\mathrm{K}} \to \infty$ we obtain a modified reduced mass $\mu'_{\mathrm{red}} = m_{\mathrm{Li}}$, which differs by a factor of 40/46 from the experimental one. This needs to be taken into account when identifying the microscopic parameters. To ensure, in particular, that the off-diagonal coupling g in Eq. (12) remains of the same strength as in the experiment, a reduced resonance parameter $R'^* = (40/46)^2 R^*$ has been used, which we do for all data shown in the main text. Using these identifications, the model Eq. (12) also accurately describes the short-time dynamics as given by Eq. (11), cf. Fig. 2 in the main text.

The calculation of time-resolved, many-body expectation values such as Eq. (9) at arbitrary temperature presents a theoretical challenge. However, for the model (12), we are able to calculate the time-resolved Ramsey response in an exact way using the FDA [11, 37]. This is based on the observation that for bilinear Hamiltonians thermal expectation values in the many-body Fock space can be reduced to determinants in the single-particle space by virtue of the identity

$$\mathrm{tr}[\hat{\rho}\; e^{\hat{Y}_1} e^{\hat{Y}_2}\ldots] = \det[1 - \hat{n} + \hat{n}\; e^{\hat{y}_1} e^{\hat{y}_2}\ldots]. \tag{13}$$

Here $\hat{Y}_1, \hat{Y}_2, \ldots$ are many-body operators, $\hat{y}_1, \hat{y}_2, \ldots$ are their single-particle counterparts, $\hat{\rho}$ is the many-body density matrix describing the state of the system, and $\hat{n} = 1/[e^{\beta(\hat{h}_0-\mu)} + 1]$ is the occupation operator defined in the single-particle space, with μ the fermion chemical potential. A specific example for Eq. (13) is the perfect quench Ramsey response, which at finite temperature is given by [11]

$$S(t) = \mathrm{tr}[\hat{\rho}\; e^{i\hat{H}_0 t} e^{-i\hat{H}t}] = \det[1 - \hat{n} + \hat{n}\; e^{i\hat{h}_0 t} e^{-i\hat{h}t}]. \tag{14}$$

Here, $\hat{H}_0 = \sum_{\mathbf{k}} \epsilon_{\mathbf{k}}\hat{c}^\dagger_{\mathbf{k}}\hat{c}_{\mathbf{k}}$ is the free Hamiltonian of the Li Fermi gas and $\hat{H}$ is the Hamiltonian in the presence of impurity scattering given in Eq. (12), while $\hat{h}_0$ and $\hat{h}$ are their single-particle counterparts. A numerical evaluation of Eq. (14) then only requires a calculation of the single particle orbitals and energies in order to obtain the single-particle determinant.

S2. ROLE OF PHYSICAL PROCESSES ON DIFFERENT TIME SCALES

The combination of both our theoretical approaches allows us to accurately model the physics at various time scales in our experiment. Making use of the fact that the FDA and the TBM differ distinctly in their treatment of multiple particle-hole excitations, the impurity mass, and finite temperature, we can use a comparison of their predictions to determine the role of these processes and effects in the many-body non-equilibrium dynamics of our experiment. To keep the analysis transparent, in this section we still assume that a perfect quench is performed.

S2.1. Multiple particle-hole excitations

In order to analyze the role of multiple particle-hole excitations, we first consider the limit of a fixed (infinitely heavy) impurity at zero temperature. In this scenario, the FDA yields the exact solution of the impurity problem. Since, in this case, the TBM only differs from the FDA by its neglect of multiple particle-hole excitations, a comparison of the predictions of the two methods allows us to isolate the effect of these excitations.

In Fig. 5 we display the predictions for the Ramsey response using the two theoretical approaches. We find that both theoretical predictions agree extremely well at short times. In particular, for both the amplitude and phase of $S(t)$, our results imply that multiple particle-hole excitations start to influence our observables at a time scale of around $6\tau_F$, and only become prominent beyond $10\tau_F$. Thus, at shorter time scales, multiple particle-hole excitations can be neglected when predicting the results of the Ramsey measurements.

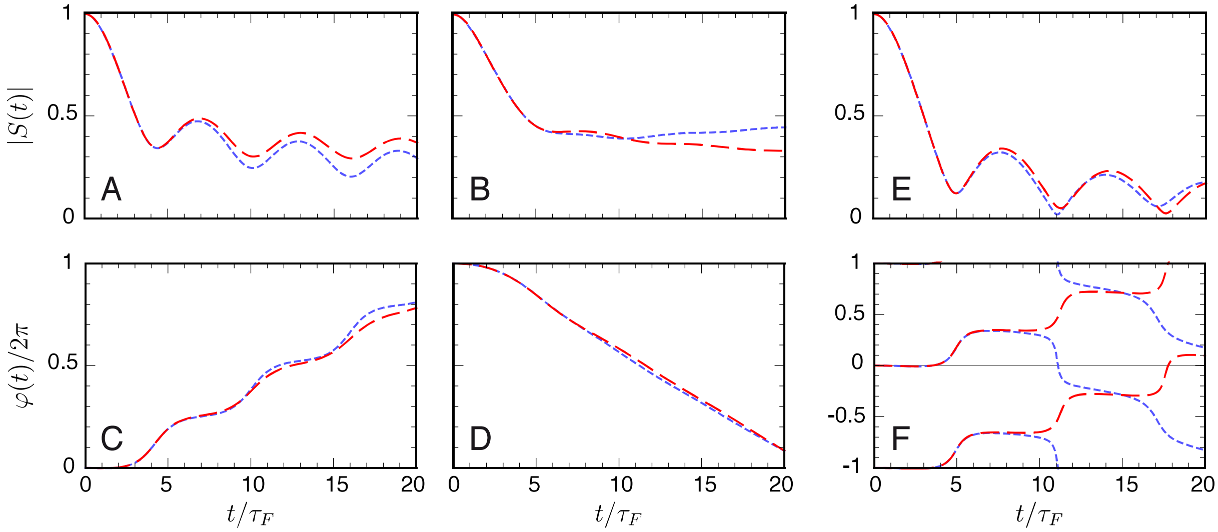

FIG. 5. **Effect of multiple particle-hole fluctuations**. Taking the idealizing limit of zero temperature and infinite impurity mass, we compare the Ramsey response for a perfect quench (top: amplitude, bottom: phase) obtained exactly with the FDA (red, long dashed) to the one obtained with TBM (blue, short dashed) for (**A**, **C**) $X = -0.23$, (**B**, **D**) $X = 0.86$, and (**E**, **F**) $X = 0.08$. For this comparison, we take $r_0 = 0$ and $k_F R'^* = 1.1(40/46)^2$.

We note that the fixed impurity scenario is a worst-case scenario for the TBM: At $T = 0$, the infinitely heavy impurity is subject to the orthogonality catastrophe with an associated power-law decay of the Ramsey contrast at long times [39]. This decay, which arises due to an infinite number of particle-hole fluctuations and which leads to a vanishing quasiparticle weight, is exactly incorporated in the FDA. By contrast, in the long-time limit, the TBM predicts the saturation of $|S(t)|$ to a constant value (see Fig. 5), corresponding to a spurious finite residue. However, for a *mobile* impurity at zero temperature, recoil becomes relevant. These recoil effects lead to the absence of the orthogonality catastrophe [38], and thus to an increased accuracy of the TBM in the case of finite impurity mass.

Generally, one expects that the relevant time scale for multiple particle-hole excitations is closely related to the Fermi time τ_F. As discussed above, we find that such excitations become relevant for a description of $S(t)$ only at around $6\tau_F$ or beyond. This observation can be understood in a twofold way. First, in the equilibrium case it was found that contact interactions in the Fermi polaron problem lead to an approximate cancellation of terms involving identical fermions, thus suppressing the emergence of multiple particle-hole fluctuations [40]. Our observation may hence be interpreted as a generalization of these findings to the non-equilibrium case. Second, the spectrum of the Fermi polaron problem features a dominant contribution involving the excitation of fermions from the bottom of the Fermi sea to the Fermi surface [11]. As discussed in Ref. [11], these excitations manifest themselves as oscillations with period $2\pi\tau_F$ in the Ramsey contrast $|S(t)|$. Such a bottom of the band excitation is also present in the truncated wavefunction (8), and indeed the remarkable agreement of the TBM with the exact solution from the FDA up to the time $2\pi\tau_F$ suggests that this effect can be captured by single-particle hole excitations.

S2.2. Impurity mass

As discussed in the main text, our experimental findings are well described by the static impurity approximation, although the impurity has finite mass. To quantify the effect of the finite impurity mass, we study here the case of zero temperature. This allows us to isolate the effect of finite impurity recoil from the influence of thermal fluctuations, which will become dominant beyond times $\tau_T \approx 6\tau_F$, as discussed in the section below. In order to estimate at which time scale recoil becomes important, we make use of the capability of the TBM to describe impurities of arbitrary mass. Furthermore, our analysis in Sec. S2.1 shows that the TBM yields highly accurate results for the short-time dynamics of $S(t)$. Accordingly, in Fig. 6 we display the Ramsey response for a static impurity and for the experimentally relevant impurity mass, both calculated within the TBM. We see that for both amplitude and phase, the impurity motion only results in a small difference in the Ramsey signal at times $t \lesssim 4\tau_F$. Physically, this time scale corresponds to the effective recoil time τ_R associated with Li collisions on K atoms, which we estimated in Sec. S1.3 to be $\tau_R \approx 4\tau_F$, in agreement with our findings here. At times exceeding τ_R, we find that the dynamics is indeed affected by the finite impurity mass. However, at such times, thermal fluctuations dominate the behavior in experiment, as we now discuss.

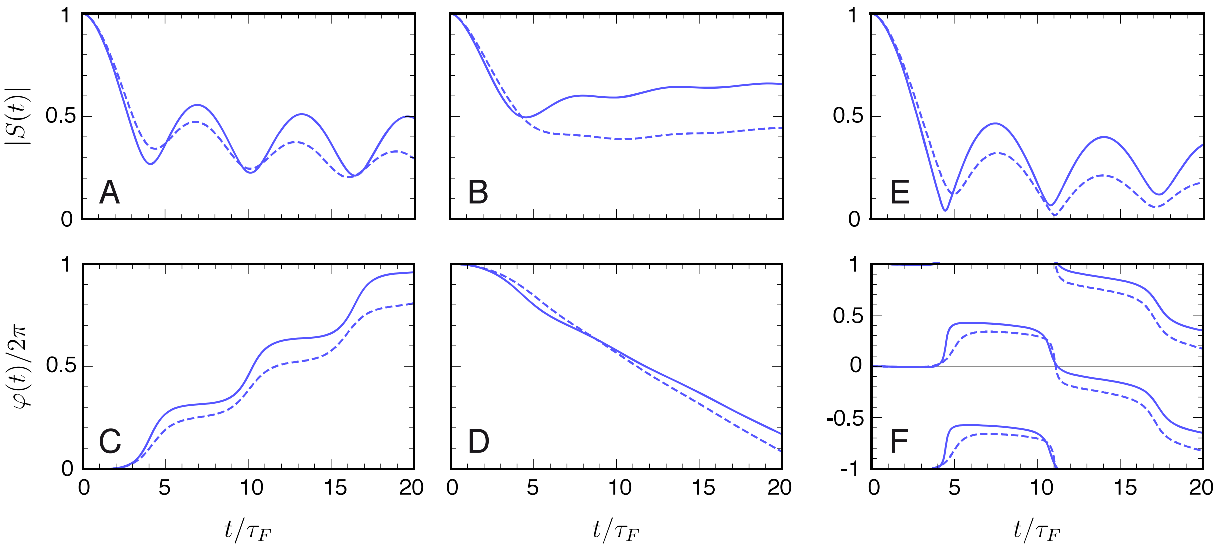

FIG. 6. **Effect of the impurity motion on the short-time dynamics.** Amplitude (top) and phase (bottom) of the perfect quench zero temperature Ramsey response $S(t)$ as a function of time for (**A**, **C**) $X = -0.23$, (**B**, **D**) $X = 0.86$, and (**E**, **F**) $X = 0.08$. We compare the results of the TBM obtained for $m_{\mathrm{K}} = (40/6)m_{\mathrm{Li}}$ and $k_F R^* = 1.1$ (solid) with the TBM results for fixed impurities $m_{\mathrm{K}} \to \infty$ and $k_F R'^* = 1.1(40/46)^2$ (dashed).

S2.3. Temperature

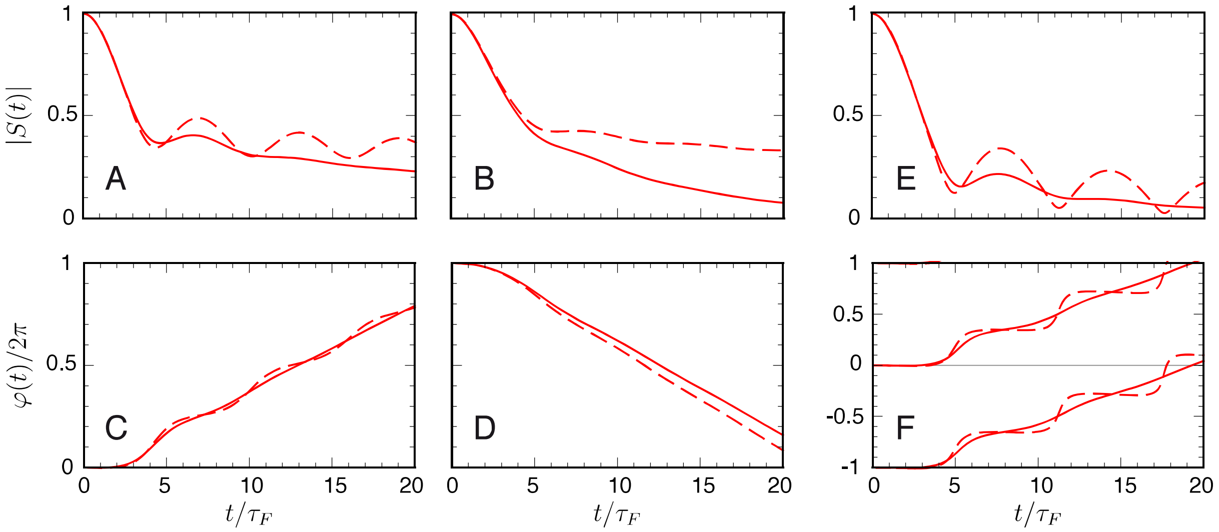

FIG. 7. **Effect of finite temperature on the impurity dynamics**. We compare the Ramsey signal (upper panels: amplitude, lower panels: phase) for an infinitely heavy impurity obtained from an exact FDA calculation at zero (long dashed) and finite temperature (solid curves). The ordering of the graphs is as in the main text: (**A**, **C**) $X = -0.23$, $T/T_F = 0.17$, (**B**, **D**) $X = 0.86$, $T/T_F = 0.16$, and (**E**, **F**) $X = 0.08$, $T/T_F = 0.18$. We assume a perfect quench and choose $r_0 = 0$ as well as $k_F R^* = 1.1$, i.e., $k_F R'^* = 1.1(40/46)^2$.

At long times, the time evolution reduces to a simple exponential decoherence of $S(t)$. The time scale at which this crossover to exponential decay takes place is given by the thermal time scale τ_T. In our experiment, where $T/T_F \approx 0.15$, this corresponds to $\tau_T \approx 6\tau_F$ and, hence, we observe both regimes within the dynamical range probed in our experiment.

In this section, we use finite-temperature FDA calculations to gauge the role of temperature in the impurity dynamics. To this end we compare the results for the Ramsey signal at zero and finite temperature for the experimentally realized parameters. The results are shown in Fig. 7. We indeed find that at times $\sim 6\tau_F$ the time evolution at finite temperature starts to deviate from the purely quantum behavior. Finite temperature leads to an exponential decoherence of the Ramsey signal and has the consequence that thermal fluctuations dominate over the impurity motion at times $t \gtrsim 6\tau_F$ [38]. Hence they mask the effect of impurity recoil as discussed in Sec. S1.3.

Overall, the conditions in our experiment give rise to three competing time scales. Multiple particle hole excitations become relevant for our measurement of $S(t)$ at around $6\tau_F$, the recoil time is $\tau_R \approx 4\tau_F$, and the thermal scale is set by $\tau_T \approx 6\tau_F$. A comparison of these scales reveals the reason for the remarkable agreement between the FDA and experiment: Recoil is only weakly probed at short times $t < \tau_R$, while its effect is washed out by the thermal fluctuations at long times $t > \tau_T \approx \tau_R$.

S3. ROLE OF INTERACTION DURING FINITE-LENGTH RF PULSES

In this section, we analyze the role of the 'imperfect' interaction quench in our experiments, where residual interactions are present during the rf pulses. Furthermore, we discuss how our findings pave the way towards the use of our experimental techniques to exert control over many-body states in real time.

S3.1. Idealized versus realized Ramsey scenario

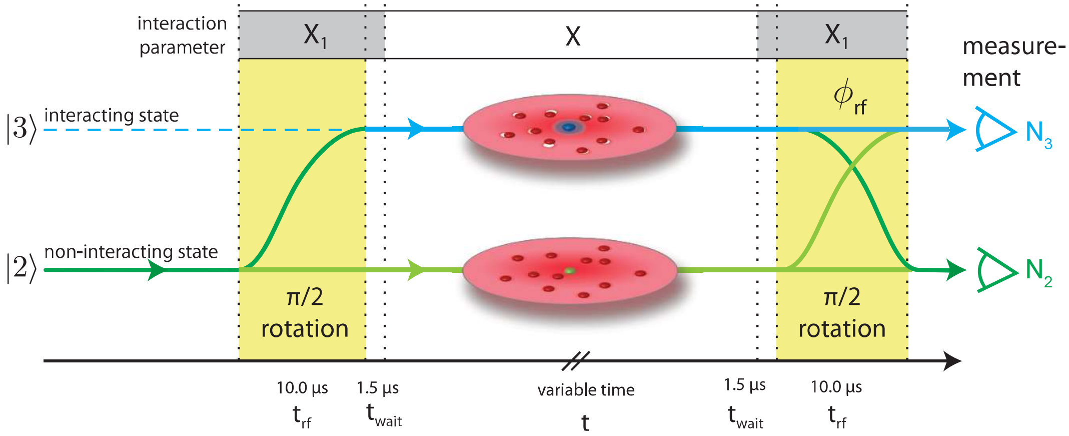

FIG. 8. **Schematic of the experimental Ramsey procedure.** The K atoms start out in the hyperfine state K$|2\rangle$, which is effectively non-interacting with the Fermi sea. A 10 μs (3.4 τ_F) long square $\pi/2$ pulse is applied in the presence of weak interactions between the K$|3\rangle$ atoms and the Li atoms, quantified by the interaction parameter X_1. We then use optical control of our Feshbach resonance to rapidly (in less than 200 ns (0.08 τ_F)) quench the system into the strongly interacting regime (interaction parameter X). After a variable interaction time t we optically shift the interaction strength back to X_1, and then close the Ramsey sequence by a second $\pi/2$ pulse. We vary the phase of this pulse by shifting the phase of the rf source by $\phi_{\rm rf}$ before the second pulse is applied.

Thus far, we have assumed the idealized scenario of a perfect two-pulse Ramsey scheme. In this case, the initial spin state of the impurity (K$|2\rangle$ in the experiment) is non-interacting with the Li Fermi sea and there are no interactions during the applied rf $\pi/2$ pulses.Each pulse then yields a perfect rotation on the Bloch sphere, e.g., the initial state K$|2\rangle$ is transformed into the spin-state superposition $(\mathrm{K}|2\rangle + \mathrm{K}|3\rangle)/\sqrt{2}$. For such a perfect Ramsey sequence, the measured Ramsey signal $S(t)$ gives the overlap between the time-evolved interacting and non-interacting states of the system [10, 11], yielding Eqs. (9) and (14) for zero and finite temperature, respectively. In this idealized scenario, the Fourier transform of $S(t)$ corresponds to the excitation spectrum of the system in linear response [41],

$$A(\omega) = \mathrm{Re} \int_0^\infty \frac{dt}{\pi} e^{i\omega t} S(t), \tag{15}$$

where ω is the frequency of the applied field.

In our experiments, however, residual interactions are present during the $\pi/2$ pulses, which take a finite time to be completed. As shown in the illustration of our experimental sequence in Fig. 8, the state K$|3\rangle$ can already interact with the Li cloud during the $\pi/2$ rotation, which potentially affects the observed dynamics of the system. Specifically, this stage of the experiment is performed at a detuning from the Feshbach resonance which corresponds to a weak interaction strength X_1 between the impurities and the Fermi sea (cf. Section S3.2 and Fig. 8). After preparing the superposition state of the impurity spin, we quench the system to strong interactions (interaction parameter X) by optically shifting the Feshbach resonance [12]. We previously focussed on the complex non-equilibrium dynamics resulting from the strong interactions X during the time t. In the following, we analyze the effect of the residual interaction X_1 during the finite-duration $\pi/2$ spin rotations. In particular, we investigate the impact of these weak interactions during the rf pulses on the Ramsey response $S(t)$ and the spectrum $A(\omega)$ as obtained from the Fourier transform Eq. (15).

S3.2. Modelling of rf pulses within TBM

In this section, we extend our modelling of the zero-temperature impurity dynamics within the TBM to directly simulate the entire experimental procedure, as illustrated in Fig. 8. In order to model the rf pulses, we explicitly include both K$|2\rangle$ and K$|3\rangle$ spin states, as well as the rf field. This modifies the Hamiltonian, Eq. (1), to $\hat{\mathcal{H}} = \hat{H} + \hat{H}_{\mathrm{rf}}$ with the additional term

$$\hat{H}_{\mathrm{rf}} = \frac{\Omega}{2i}\sum_{\mathbf{k}}\left(e^{i\phi_{\mathrm{rf}}}\hat{d}^{\dagger}_{\mathbf{k},2}\hat{d}_{\mathbf{k},3} - e^{-i\phi_{\mathrm{rf}}}\hat{d}^{\dagger}_{\mathbf{k},3}\hat{d}_{\mathbf{k},2}\right) + \sum_{\mathbf{k}}(\epsilon_{\mathbf{k},\mathrm{K}} + \hbar(\omega_{\mathrm{rf}} - \omega_0))\hat{d}^{\dagger}_{\mathbf{k},2}\hat{d}_{\mathbf{k},2}. \tag{16}$$

Here, we have used the rotating wave approximation. Ω corresponds to the strength of the rf field, ϕ_{rf} is the variable phase of the second rf pulse, and $\hat{d}^{\dagger}_{\mathbf{k},\sigma}$ creates a particle in the state K$|\sigma\rangle$ with momentum $\hbar\mathbf{k}$. Note that $\hat{d}^{\dagger}_{\mathbf{k}} \equiv \hat{d}^{\dagger}_{\mathbf{k},3}$ in the original two-channel Hamiltonian (1). The interactions during the rf pulses cause a shift in the transition frequency between the K$|2\rangle$ and K$|3\rangle$ states from the bare transition frequency ω_0 to $\omega_0 + \varepsilon_1/\hbar$, where ε_1 is the polaron energy at interaction parameter X_1. As described in Sec. S5.B, we account for this shift by adjusting the frequency of our rf pulses to $\omega_{\mathrm{rf}} = \omega_0 + \varepsilon_1/\hbar$.

According to the last term in Eq. (16), the shift in the frequency of the rf source from ω_0 to ω_{rf} causes the observed signal to accumulate an additional phase $(\omega_{\mathrm{rf}} - \omega_0)t$ during the interaction time t. To account for this, we introduce the phase $\phi = \phi_{\mathrm{rf}} + (\omega_{\mathrm{rf}} - \omega_0)t$. We then determine $|S(t)|$ and the phase $\varphi(t)$ by noting that the Ramsey signal $(N_3 - N_2)/(N_3 + N_2)$ corresponds to a sine-wave function of ϕ plus an offset, i.e., it takes the form $F(t) + |S(t)|\cos(\phi - \varphi(t))$ with $F(t)$ a real, ϕ-independent function. This mirrors the experimental procedure, where $F(t)$, $|S(t)|$, and $\varphi(t)$ appear as fit-parameters for the Ramsey signal, see Sec. S5.B.

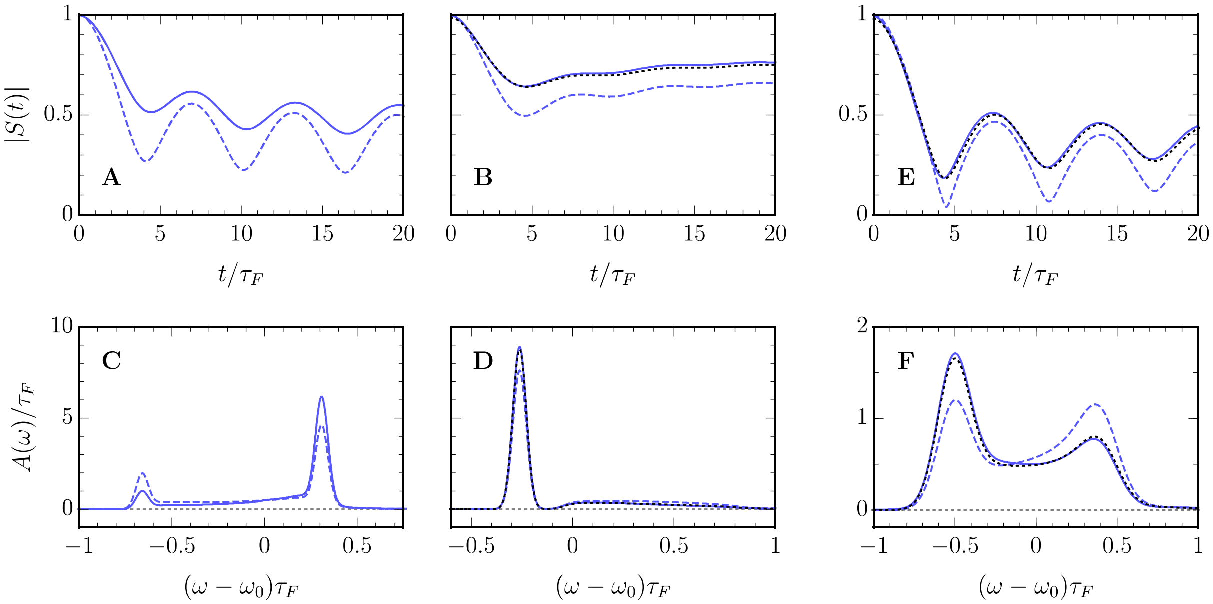

FIG. 9. **Role of the residual interactions within TBM.** We present the zero-temperature response $S(t)$ and the corresponding spectrum $A(\omega)$ for the perfect quench (dashed blue) and the actual experimental sequence shown in Fig. 8 (solid blue). As in the main text, we take $k_F R^* = 1.1$ and the interaction parameters: (**A**, **C**) $X = -0.23$, $X_1 = -3.9$, (**B**, **D**) $X = 0.86$, $X_1 = 5.8$, and (**E**, **F**) $X = 0.08$, $X_1 = 4.8$. For comparison, in (**B**, **D**, **E**, **F**), we represent by black dotted lines the scenario where the initial state before the quench is approximated as a weakly attractive polaron — see Sec. S3.2 for details. The spectra have been convolved with the experimental Fourier-limited rf spectral lineshapes, which are Gaussian-shaped with width σ, where $\sigma\tau_F = 0.03$ for $X = 0.86, -0.23$, and $\sigma\tau_F = 0.1$ for $X = 0.08$.

Within the TBM, we determine the approximate eigenstates and eigenvalues of $\hat{\mathcal{H}}$ within the more general class of truncated wavefunctions:

$$|\psi_{\rm rf}\rangle = \left(\alpha_{0,3}\hat{d}^\dagger_{0,3} + \alpha_{0,2}\hat{d}^\dagger_{0,2}\right)|{\rm FS}\rangle + \sum_{\mathbf{q}} \alpha_{\mathbf{q}} \hat{b}^\dagger_{\mathbf{q}} \hat{c}_{\mathbf{q}} |{\rm FS}\rangle + \sum_{\mathbf{kq}} \left(\alpha_{\mathbf{kq},3} \hat{d}^\dagger_{\mathbf{q}-\mathbf{k}\downarrow} \hat{c}^\dagger_{\mathbf{k}} \hat{c}_{\mathbf{q}} + \alpha_{\mathbf{kq},2} \hat{d}^\dagger_{\mathbf{q}-\mathbf{k},2} \hat{c}^\dagger_{\mathbf{k}} \hat{c}_{\mathbf{q}}\right)|{\rm FS}\rangle \,.$$

To model the experimental quench sequence illustrated in Fig. 8, we apply a series of time evolution operators to the initial state consisting of a K$|2\rangle$ atom and the Li Fermi sea. At the end of the sequence we then extract the number of K atoms in states K$|2\rangle$ and K$|3\rangle$, respectively. We include explicitly the rf pulses, the wait times, and the interaction time t during which the system is strongly interacting. The results of this procedure are displayed in Fig. 2 of the main text. Here, we account for slight additional experimental decoherence by scaling the prediction for $|S(t)|$ as described in Section S.5C.

In the upper panels of Fig. 9 we compare the Ramsey response obtained by simulating the actual experimental sequence (solid line) with that of the perfect quench scenario (dashed line). We see that the residual interactions X_1 in experiment can indeed influence the quantum evolution of the impurity. The difference in the responses can be straightforwardly explained by assuming that the main effect of X_1 is to produce a weakly interacting initial state. Specifically, for weak attractive interactions $X_1 > 0$, the Ramsey response can be approximated as

$$S(t) \simeq Z \, \langle\psi_{X_1}| \, e^{-i\hat{H}t/\hbar} \, |\psi_{X_1}\rangle \,, \tag{17}$$

where $|\psi_{X_1}\rangle$ is the ground state of the Hamiltonian (1) at interaction parameter X_1, and Z is the corresponding polaron residue. Note that we cannot formally construct a similar expression for the repulsive case $X_1 < 0$, since the repulsive polaron is a metastable state, involving multiple eigenstates of the Hamiltonian.

Referring to Fig. 9, the excellent agreement between the approximation (17) and the full Ramsey signal provides strong evidence that the residual interactions X_1 produce a weakly attractive initial state. This is further supported by the spectrum $A(\omega)$ shown in the bottom panels, where we see that the residual interactions enhance the attractive polaron peaks for $X = 0.08$ and 0.86. A similar enhancement of the repulsive polaron peak is observed for $X = -0.23$. Hence we conclude that the explicit modelling of the impurity dynamics using the full Hamiltonian $\hat{\mathcal{H}} = \hat{H} + \hat{H}_{\rm rf}$ is not essential for the description of the dynamics during the initial $\pi/2$ spin rotation and instead one can fully describe the time evolution using the Hamiltonian (1).

S3.3. Modelling of experimental procedure at finite temperature within FDA

The interplay between the residual interactions and finite temperature presents a further theoretical challenge. In the following, we use the FDA to simulate the experimental protocol (Fig. 8) at finite temperature. To achieve this, we exploit the finding from Sec. S3.2 that the detailed dynamics of the rf-driven oscillations between the K$|2\rangle$ and K$|3\rangle$ states can be ignored when calculating $S(t)$. Thus, we assume that the initial $\pi/2$ rotation effectively produces a spin superposition $({\rm K}\,|2\rangle + {\rm K}\,|3\rangle)/\sqrt{2}$, independently of the residual interaction X_1 of the impurity in the state K$|3\rangle$ with the Fermi sea. To account for the dynamics due to the weak interaction X_1, we then let the system evolve under this interaction for a hold time $t_{\rm h} = t_{\rm rf}/2 + t_{\rm wait}$, which models the dynamics at weak interaction X_1 as the result of a sudden switch-on of this interaction at the midpoint of the $\pi/2$ pulses. After the hold time $t_{\rm h}$, the final quench to the strong interactions X is performed. For the measurement of the Ramsey contrast, this sequence is reversed. Theoretically, this yields the modified time-dependent overlap

$$S(t) = {\rm tr}\left[\hat{\rho}\, e^{i\hat{H}_0(2t_{\rm h}+t)} e^{-i\hat{H}_1 t_{\rm h}} e^{-i\hat{H}_X t} e^{-i\hat{H}_1 t_{\rm h}}\right], \tag{18}$$

where $\hat{H}_1$ and $\hat{H}_X$ denote the Hamiltonian (1) at interaction strength X_1 and X, respectively. Using the FDA, the expression Eq. (18) is evaluated exactly according to Eq. (13) at the experimental temperature. As can be inferred from Eq. (18), this simplified model of the experimental protocol corresponds to a sequence of interaction quenches.

In the upper panel of Fig. 10 we compare the result for $|S(t)|$ at the experimental temperatures obtained for the experimental sequence (solid lines) to the result for an idealized, i.e., perfect quench, Ramsey sequence (dashed lines). Similarly to the case of zero temperature, we see that the time evolution at X_1 has an experimentally observable effect on the dynamics. In particular, it generates an additional decoherence of the Ramsey signal already at $t = 0$, as well as an enhancement of the oscillations in $|S(t)|$ for resonant interactions – see Fig. 10E.

For the calculation of the FDA results shown in Fig. 2 of the main text we use the same procedure as described above. We account for slight additional experimental decoherence by scaling the prediction for $|S(t)|$ as described in Section S.5C. We also note that the phase $\varphi_{\rm FDA}(t)$ of the Ramsey signal $S(t) = |S(t)|e^{-i\varphi_{\rm FDA}(t)}$, as determined from

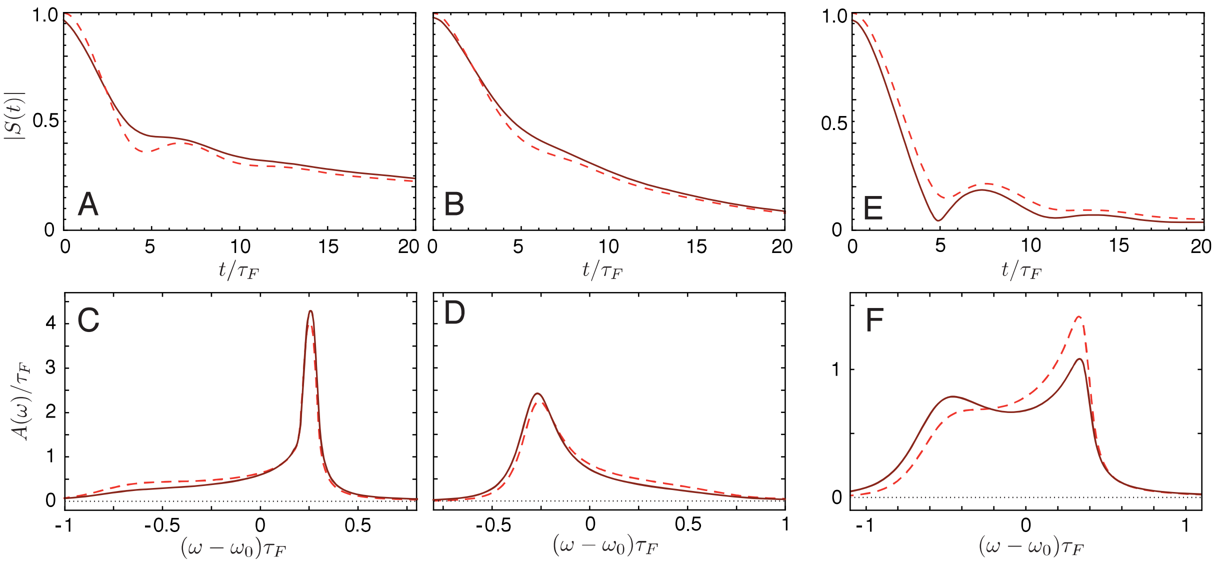

FIG. 10. **Role of the residual interactions in the Ramsey sequence at finite temperature**. Upper panels: we compare the perfect quench Ramsey response (dashed) with a simulation of the experimental sequence (solid). Lower panels: we compare the linear-response excitation spectrum (dashed) with the Fourier transform of the signal obtained using the experimental sequence (solid). As in the main text, we take $k_F R^* = 1.1$ and the interaction parameters: (**A**, **C**) $X = -0.23$, $X_1 = -3.9$, (**B**, **D**) $X = 0.86$, $X_1 = 5.8$, and (**E**, **F**) $X = 0.08$, $X_1 = 4.8$. The temperatures are $T/T_F = 0.166$, 0.158, 0.177, respectively.

Eq. (18), differs from the experimentally measured phase $\varphi(t)$ due to the detuning of the rf frequency from ω_0. They are related by $\varphi(t) = \varphi_{\mathrm{FDA}}(t) - (\omega_{\mathrm{rf}} - \omega_0)(2t_{\mathrm{wait}} + t_{\mathrm{rf}})$. Similar to the previous section and to the experiment, we take $\omega_{\mathrm{rf}} - \omega_0 = \varepsilon_1/\hbar$.

As outlined in Section S3.1, in the idealized Ramsey scenario the Fourier transform $A(\omega)$ of $S(t)$ is equivalent to the rf absorption in linear response, cf. (15) [11]. Similarly to our $T = 0$ analysis in Sec. S3.2, we now study the effect of the residual interactions X_1 on the spectral decomposition of $S(t)$. To this end we compare the two signals $A(\omega)$ for the perfect quench with the result obtained for the experimental sequence as modelled by Eq. (18). We show the comparison of the spectra obtained in the idealized (dashed) and experimentally realized scenario (solid) in the lower panel of Fig. 10. As for our $T = 0$ results discussed above, we find only a small difference between the two finite-temperature spectra. Therefore, in agreement with the experimental observation, cf. Fig. 3 in the main paper, under the condition of $|X_1| \approx 5$ we see that the weak interactions during the rf pulses have an observable but small effect on the predicted spectra.

In accordance with the results from the TBM shown in Fig. 9, we find from the evaluation of Eq. (18) that weak interactions X_1 lead to a small shift of spectral weight into the corresponding dominant polaron branches. This shift of spectral weight is also observed experimentally, see Fig. 3 of the main text.

S3.4. Stronger interactions during rf pulses: illustration of quantum state preparation

The shift of spectral weight towards the attractive or repulsive branches of the spectrum, cf. Figs. 9 and 10, may be interpreted as follows: The residual interactions present during the initial $\pi/2$ impurity spin rotation serve to produce an interacting many-body quantum state. As such, this procedure can be viewed as an adiabatic preparation of an attractive or repulsive polaron. Compared to the noninteracting state, this polaron has an increased wavefunction overlap with the corresponding branch of the strongly interacting system. When the system is then quenched into the regime of strong interactions, the increased overlap results in the corresponding shift of the spectral weight. An intriguing question is then whether such an approach can provide a novel way to experimentally control the spectral decomposition of quantum states.

To investigate this possibility, we increase the interaction during the $\pi/2$ rotations, corresponding to decreasing $|X_1|$, and determine the effect on $A(\omega)$. In the upper panel of Fig. 11 we show the spectra obtained by linear-response rf spectroscopy (green squares). Similar to Fig. 3 of the main paper, we compare this result to the Fourier transform of the Ramsey signal $S(t)$ (gray shading), as obtained from the experimental sequence described in Fig. 8. We also compare our experimental result to the prediction from the FDA, where the dynamics has been modelled as described

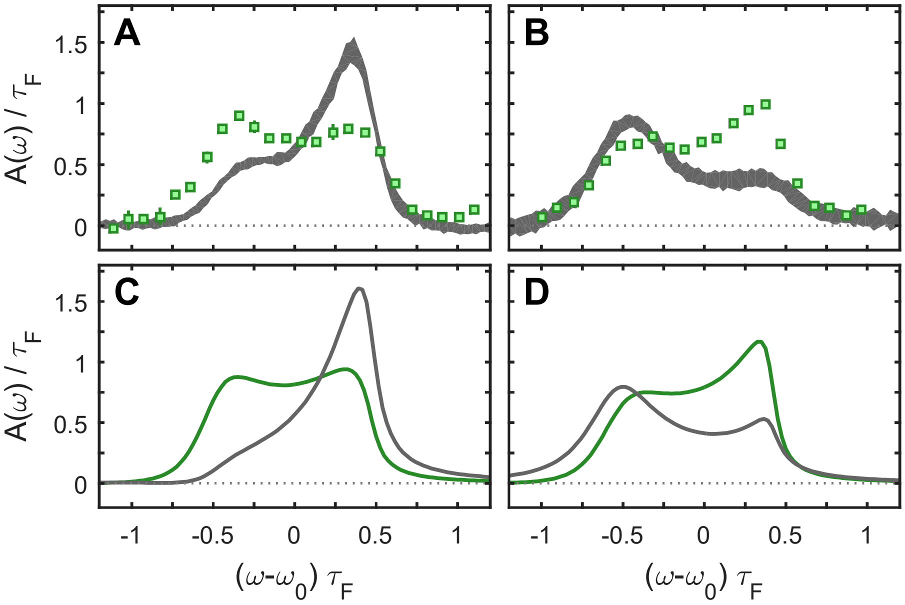

FIG. 11. **Control of the spectral decomposition of many-body quantum states.** Upper panel: We compare the experimentally measured rf spectrum at the interaction parameter X (green squares) to the Fourier transform of $S(t)$ obtained using the measurement procedure illustrated in Fig. 8 with initial interaction parameter X_1 (gray shading). Lower panel: we compare the theoretical prediction from the FDA for the linear-response excitation spectrum (green) to the Fourier transform of the signal obtained by simulating the experimental sequence according to Eq. (18). (**A**, **C**) $X = 0.14$, $X_1 = -2.2$, $k_F R^* = 1.09$, $T/T_F = 0.174$. (**B**, **D**) $X = -0.25$, $X_1 = 1.7$, $k_F R^* = 1.1$, $T/T_F = 0.17$.

by Eq. (18). As in the main text, we find excellent agreement between experiment and theory. Indeed, both feature a strong shift of spectral weight to regions of the spectrum that are adiabatically connected to the dominant polaron branches at interaction X_1. Furthermore, when comparing $A(\omega)$ in Fig. 11, with the spectrum for $|X_1| \approx 5$ in Figs. 9 and 10, it is clear that the amount by which the spectrum is shifted can be controlled by the strength of the interaction during the rf pulses. This strongly supports the assertion that the initial interactions can be used to precisely control the many-body dynamics. Our experimental techniques thus allow for a precise, dynamic control of the spectral decomposition of quantum states in future experiments.

The excellent agreement between theory and experiment also demonstrates that our theoretical approaches can be used to explore experimental ramps in combination with interferometric protocols in order to find, for instance, optimized spin and interaction trajectories.

S4. UNIVERSAL FEATURES OF IMPURITY DYNAMICS AND RELATION TO ORTHOGONALITY CATASTROPHE

For impurities localized in space, which, for instance, can be achieved by species-selective three dimensional optical lattices, our experimental setup allows one to study universal features exhibited by the Anderson orthogonality catastrophe [39]. The orthogonality catastrophe was originally studied in the context of x-ray absorption spectra in metals, where high-energy x-ray photons create atomic core holes by photoemission of inner-shell electrons [41]. These core holes produce a scattering potential for the electrons in the conduction band, leading to characteristic power-law edges in the absorption spectra with an exponent that is universally determined by the scattering phase shift at the Fermi surface [39]. However, impurities, phonons, residual interactions between the electrons, and a lack of knowledge of microscopic parameters makes it difficult to unambiguously determine the universal features of the orthogonality catastrophe in typical solid state materials [42]. In contrast, the Hamiltonian in our experiment is well characterized on all relevant energy scales, and therefore the full dynamic response of the system can be reliably calculated by theory and probed by the ultrafast experimental techniques demonstrated in this work. This enables one to obtain fundamental insights into universal features of the orthogonality catastrophe, which are difficult to access in other systems.

To illustrate how the orthogonality catastrophe would manifest itself in an ultracold atomic gas experiment, the response of infinite mass impurities calculated using the FDA for the perfect quench scenario is shown in Fig. 12. First, at short times and for a range parameter of the Feshbach resonance $R^* > 0$, we see that the Ramsey contrast

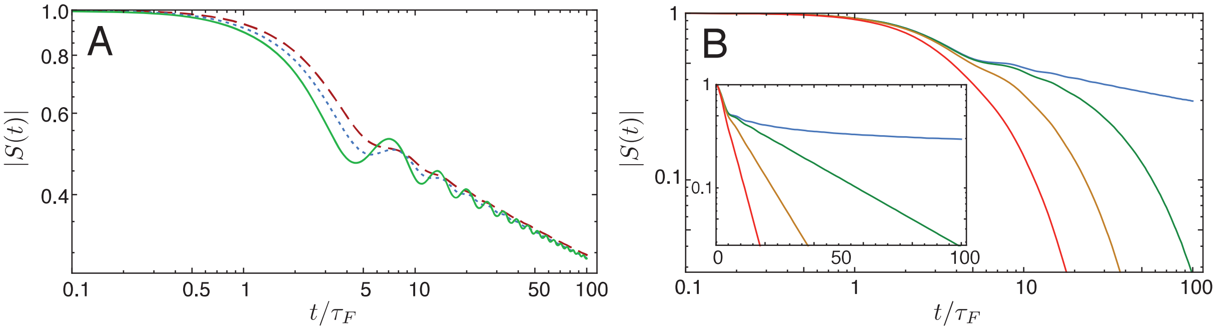

FIG. 12. **Universal features of the dynamical orthogonality catastrophe**. We show the Ramsey contrast for an infinitely heavy impurity obtained within the FDA. (**A**) The zero-temperature Ramsey contrast exhibits a power law decay, shown on a double logarithmic scale. We change the Feshbach resonance range $k_F R^*$ and interaction parameter X in such a way that the scattering phase shift at the Fermi surface is constant leading to a constant exponent of the power law tail. The data corresponds to a fixed phase shift $\delta_{k_F} = 1.4$ with the choices $(X, k_F R^*) = (1, 1.12)$ (dashed red), $(X, k_F R^*) = (0.58, 0.56)$ (dotted blue), and $(X, k_F R^*) = (0.15, 0)$ (solid green). (**B**) Ramsey contrast at various temperatures on a double logarithmic scale. We choose temperatures $T/T_F = 0$ (blue), 0.05 (green), 0.15 (orange), 0.4 (red) at fixed values $X = 1$ and $k_F R^* = 1.12$. The inset shows the same data on a logarithmic-linear scale to emphasize the appearance of exponential tails at finite temperature.

decays quadratically for all scattering parameters and temperatures considered, in accordance with Eq. (11). The main universal feature associated with the orthogonality catastrophe is expected in the long-time dynamics at $T = 0$: Here, the Ramsey response is predicted to exhibit power law tails, which depend only on the scattering phase shift at the Fermi surface [11, 39]. This is explicitly verified in Fig. 12A where we fix the scattering phase shift at the Fermi surface but change the scattering parameters. While the response at intermediate times depends on the scattering parameters, we see that the long-time evolution approaches a universal power law that only depends on the phase shift at the Fermi surface. We note that the long-time dynamics is universal: It is the same for a system with a broad resonance where $R^* = 0$ (solid line in Fig. 12A), as it is for our system with a finite range parameter (dashed and dotted lines).

When the temperature is non-zero, as in the experiment, thermal fluctuations alter the power law dephasing dynamics at sufficiently long times. Instead, exponential tails due to thermal decoherence appear as another universal feature of the dynamics [11, 39, 43, 44]. The exponential tails are illustrated in Fig. 12B. The effects of thermal decoherence could be countered by employing the recently developed cooling methods [25], opening the door to observing the orthogonality catastrophe in a cold-atom system.

Finally, we note that in our experiment temperature becomes relevant at a time scale similar to those associated with recoil and multiple particle-hole excitations. It is a challenge for theoretical approaches to exactly account for both recoil and higher order particle-hole excitations [38]. However, experiments at lower temperatures which take advantage of the tunability of the impurity mass using optical lattices would be ideally suited to probe the competition between these effects. Such ultracold-atom experiments would hence provide important insight into this long standing theoretical question.

S5. EXPERIMENTAL AND DATA ANALYSIS PROCEDURES

In this section we discuss the procedures used to record and analyze the data presented in this work. We detail the cooling and preparation of our atomic samples, the details of the rf pulses used in our Ramsey sequences, the methods used to analyze the data and the method that we use to vary the concentration of the K atoms.

S5.1. Sample preparation

The atomic samples are prepared by forced evaporation of Li atoms from a Li-K mixture held in an optical trap, where the K atoms are sympathetically cooled by the Li environment. This preparation procedure is described in detail in Refs. [45, 46]. At the end of the forced evaporation, the Li and K atoms are transferred into an optical trap composed of two crossed 1064-nm laser beams, as described in Ref. [12]. The measured radial and axial trap frequencies of the Li atoms are $f_{r,\mathrm{Li}} = 941(5)$ Hz and $f_{z,\mathrm{Li}} = 134(1)$ Hz, respectively. The measured radial and axial trap frequencies of the K atoms are $f_{r,\mathrm{K}} = 585(3)$ Hz and $f_{z,\mathrm{K}} = 81(1)$ Hz, respectively.

Figure(s)	N_{Li} (10^5)	N_{K} (10^4)	T (nK)	ϵ_F/h (kHz)	$\frac{\sigma(E_F)}{\epsilon_F}$ %	$\bar{n}_{\mathrm{Li}}$ $10^{12}\mathrm{cm}^{-3}$	$\bar{n}_{\mathrm{K}}$ $10^{12}\mathrm{cm}^{-3}$
2A, 2C, 3A	3.5(4)	0.95(10)	435(25)	54.6(2.7)	7.4	8.9(7)	1.8(3)
2B, 2D, 3B	3.3(4)	1.0(1)	410(25)	53.9(2.4)	7.1	8.7(6)	2.0(3)
2E, 2F, 3C	3.5(4)	1.0(1)	460(30)	54.1(2.4)	7.7	8.8(6)	1.7(3)
11A	3.1(4)	1.0(1)	430(30)	52.0(2.9)	7.7	8.2(7)	1.8(3)
11B	2.9(3)	1.05(10)	425(35)	50.8(2.1)	7.7	8.0(6)	2.0(3)
4	2.35(30)	2.5(1)	520(25)	44.2(2.3)	10.4	6.5(5)	3.4(3)

TABLE I. The total number of the Li atoms N_{Li}, the total number of the K atoms N_{K}, the sample temperature T, the effective Li Fermi energy ϵ_F, the standard deviation $\sigma(E_F)$ of the local Li Fermi energy across the trap, the trap-averaged Li and K number densities $\bar{n}_{\mathrm{Li}}$ and $\bar{n}_{\mathrm{K}}$ in our measurements.

At the end of the preparation procedure, the Li and the K atoms are in their lowest Zeeman states $\mathrm{Li}|1\rangle$ and $\mathrm{K}|1\rangle$. Before the Ramsey sequence, the K atoms are transferred to the $\mathrm{K}|2\rangle$ state using an rf pulse. Following this rf transfer, the Li and K atoms are thermalized by holding them for 750 ms in the crossed-beam optical trap. While the interaction between the $\mathrm{Li}|1\rangle$ and $\mathrm{K}|2\rangle$ atoms, characterized by the scattering length $a_{12} = 63a_0$ [14], is sufficient to ensure thermalization during this hold time, it can be neglected during the Ramsey experiments. The temperature of the atoms is determined by releasing the atoms from the trap and observing the free expansion of the K cloud.

Due to the Li Fermi pressure and the more than two times stronger optical potential for K, the K cloud is much smaller than the Li cloud [45], and therefore samples a nearly homogeneous Li environment. Because of the small variation of the Li environment sampled by the K atoms, we introduce the effective Li Fermi energy ϵ_F as

$$\epsilon_F = \frac{1}{N_{\mathrm{K}}} \int E_F(\mathbf{r}) n_{\mathrm{K}}(\mathbf{r}) d^3\mathbf{r} \,. \tag{19}$$

Here, $n_{\mathrm{K}}(\mathbf{r})$ is the local K number density at position $\mathbf{r}$ in the trap, and

$$E_F(\mathbf{r}) = \frac{\hbar^2 \left(6\pi^2 n_{\mathrm{Li}}(\mathbf{r})\right)^{2/3}}{2m_{\mathrm{Li}}} \tag{20}$$

is the local Li Fermi energy as determined by the local Li number density $n_{\mathrm{Li}}(\mathbf{r})$. We quantify the small inhomogeneity of the Li environment experienced by the K atoms by the standard deviation of the local Li Fermi energy

$$\sigma(E_F) = \left(\frac{1}{N_{\mathrm{K}}} \int (E_F(\mathbf{r}) - \epsilon_F)^2 n_{\mathrm{K}}(\mathbf{r}) d^3\mathbf{r}\right)^{1/2} \,. \tag{21}$$

We also introduce the average Li and K number densities $\bar{n}_{\mathrm{Li}}$ and $\bar{n}_{\mathrm{K}}$ sampled by the K atoms as

$$\bar{n}_{\mathrm{Li,K}} = \frac{1}{N_{\mathrm{K}}} \int n_{\mathrm{Li,K}}(\mathbf{r}) n_{\mathrm{K}}(\mathbf{r}) d^3\mathbf{r} \,. \tag{22}$$

In contrast to the Li atoms, the K atoms in our measurements remain non-degenerate, with $k_B T / E_F^{\mathrm{K}}(0) > 1.2$, where $E_F^{\mathrm{K}}(0)$ is the local potassium Fermi energy in the center of the trap when all K atoms are in the same internal state.

For all measurement presented in this work, Table I lists the total numbers of the Li and K atoms, their temperatures and trap-averaged densities, as well as the effective Li Fermi energies and their standard deviations. Throughout our measurements, these parameters remain nearly constant, with the exception of the measurements shown in Fig. 4. Here, in order to investigate the effect of the K concentration, the total number of the K atoms is increased from about 1×10^4 to 2.5×10^4. The attendant increase in the thermal load during the Li evaporation results in a decrease of the Li atom number and an increase in the temperature of the final atomic sample.

Note that, in contrast to our previous work [12], our present experiments have been optimized for large optically induced interaction shifts ($|X - X_1| \approx 5$). These shifts are produced by switching one of the crossed trapping beams from a beam with a low peak intensity and small size to a beam with a large intensity and large size propagating in the same direction. In our previous work [12], as well as in the measurements shown in Fig. 11, the waists, positions and intensities of the two beams are adjusted so as to yield mode-matched trapping potentials, preventing excitations of the center-of-mass and breathing collective modes of the atomic clouds. In the measurements presented in Figs. 2, 3 and 4, a larger beam intensity was used in order to produce a larger optical shift, resulting in some excitation of the breathing modes.

The maximal interaction time in our Ramsey measurements of 60 μs is much smaller than the shortest period of a collective oscillation (about 500 μs). We calculate that, during our short interaction time, the oscillations of the breathing modes cause at most a 6% variation of ϵ_F around its initial value specified in Table I, without any significant effect on the measurements presented here.

S5.2. Rf pulses

We apply rf pulses in the Ramsey procedures by discretely gating a continously running rf source. To record the atomic populations N_3 and N_2 as a function of the phase of the second rf pulse, we change the phase of the rf source by a variable amount ϕ_{rf} before applying this pulse.

The weak interactions between the K atoms in the K$|3\rangle$ state and the Li atoms corresponding to the interaction parameter X_1 cause the transition frequency between the K$|2\rangle$ and the K$|3\rangle$ states to differ from the transition frequency ω_0 in the absence of the Li atoms. We compensate for this effect by adjusting the frequency ω_{rf} of the rf source to be resonant with the K$|2\rangle$–K$|3\rangle$ transition at the time when the rf pulses are applied. For the data in Figs. 2A, 2B, 2C, $(\omega_{\mathrm{rf}} - \omega_0)\tau_F$ is equal to $+0.06$, -0.07, -0.05, respectively. For the data in Fig. 11C and 11D where the interaction of the K atoms during the rf pulses is stronger, $(\omega_{\mathrm{rf}} - \omega_0)\tau_F$ is equal to $+0.11$ and -0.16.

The shift in the frequency of the rf source from ω_0 to ω_{rf} causes the signal $S(t)$ to accumulate an additional phase $(\omega_{\mathrm{rf}} - \omega_0)t$ during the interaction time t. To account for this added phase, we introduce the phase $\phi = \phi_{\mathrm{rf}} + (\omega_{\mathrm{rf}} - \omega_0)t$.

S5.3. Analysis methods

We determine the contrast $|S(t)|$ and the phase $\varphi(t)$ by fitting the Ramsey signal $(N_3 - N_2)/(N_3 + N_2)$ as a function of the phase ϕ to a sine wave with an offset i.e. $F(t) + |S(t)| \cos(\phi - \varphi(t))$. Decoherence during the rf pulses, as well as imperfections of the rf pulses and the atom detection, cause the contrast for $t = 0$ to be slightly smaller than unity. When comparing theoretical results from Figs. 9 and 10 to the experimental data in Fig. 2, we account for this effect by scaling the theoretical predictions for $|S(t)|$ by an overall factor η. For each calculation, this factor is determined by fitting the prediction for $|S(t)|$ to the three data points with the the shortest interaction times. We obtain $0.92 < \eta < 1$, which corresponds to an additional loss of contrast that is of the same order as the decoherence during the rf pulses predicted by the FDA (see Fig. 10).

To compute the Fourier transform of the experimental $S(t)$ data, we use piecewise linear interpolations of $\log S(t)$ and $\varphi(t)$ between the individual data points. Outside of the range of the data, we set $S(t) = 0$. To determine the error of the Fourier transform, we sample the values of $S(t)$ and $\varphi(t)$ at each data point from Gaussian distributions whose means and standard deviations correspond to the measured values and errors, respectively. We use the standard deviation of the computed values of the Fourier transform for each value of ω as an estimate of the error indicated by the shaded areas in Figs. 3 and 11.

S5.4. Varying the K concentration

We study the effects of the impurity concentration by varying the number of the strongly interacting K atoms. If this were done by changing the total number of the K atoms in the experiment, the change in the thermal load on the Li atoms during forced evaporation would result in a correlated variation in the number of Li atoms and the sample temperature (compare the settings for Fig. 2 and Fig. 4 in Table I). To avoid these systematic effects, in the measurements presented in Fig. 4, we keep the total number of the K atoms constant and vary the fraction of the K atoms that participate in the Ramsey sequence. We accomplish this by changing the intensity of the rf pulse that transfers the K atoms from the $|1\rangle$ state to the $|2\rangle$ state before the Ramsey procedure. During the subsequent 750 ms preceding the Ramsey sequence, the K atoms collisionally thermalize with the much larger Li cloud, resulting in an incoherent mixture of K$|1\rangle$ and K$|2\rangle$ atoms at a constant temperature. When referring to these measurements, we use $\bar{n}_{\mathrm{K}}$ not for the average density of all K atoms, but for the density of those K atoms that participate in the Ramsey sequence.

We minimized the small effects of long-time drifts in the temperature, the atom numbers and the trapping potential by varying the experimental parameters in a specific order. For each K concentration and interaction time, we recorded data for 4 different phases of the second rf pulse in order to obtain $S(t)$. For each interaction time, the data with different K concentrations were recorded in immediate succession. The data sets for different interaction times were then recorded in a random order.

S6. LINEARITY OF RF RESPONSE

The response of atoms to an applied rf field is linear if the fraction of the atoms transferred from one state to another is proportional to the intensity of the field. Linearity can be ensured by using a sufficiently weak rf pulse that is also much longer than the inverse width of the relevant spectral features. The narrowest spectral features in the present work are the polaron peaks in Figs. 3A and 3B with rms widths $0.06\,\hbar/\tau_F$ and $0.09\,\hbar/\tau_F$, respectively. To record these polaron spectra, we used Blackman-shaped rf pulses [47] whose duration $t_{\rm rf} = 300\,\mu$s $\approx 100\,\tau_F$ is much longer than the inverse widths of the polaron peaks.

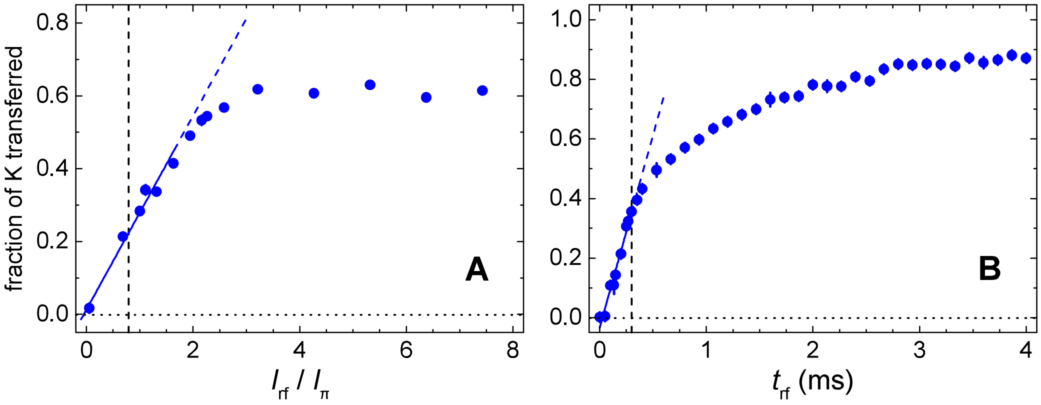

FIG. 13. **Linearity of the rf response in the repulsive polaron regime**. (**A**) Fraction of the K atoms transferred from state K$|2\rangle$ to the state K$|3\rangle$ for $X = -0.13(6)$ as a function of the intensity $I_{\rm rf}$ of an rf pulse with duration $t_{\rm rf} = 300\,\mu$s. (**B**) Fraction of the K atoms transferred for $X = -0.23(6)$ as a function of the duration $t_{\rm rf}$ of the rf pulse for the rf pulse intensity $I_{\rm rf} = 0.79\,I_\pi$. Vertical dashed lines correspond to $I_{\rm rf} = 0.79\,I_\pi$ and $t_{\rm rf} = 300\,\mu$s, respectively. The pulse frequencies are adjusted to resonantly excite the repulsive polaron. The blue solid lines indicate linear fits to the data in the ranges indicated by the same lines. The blue dashed lines show extrapolations of these fits.

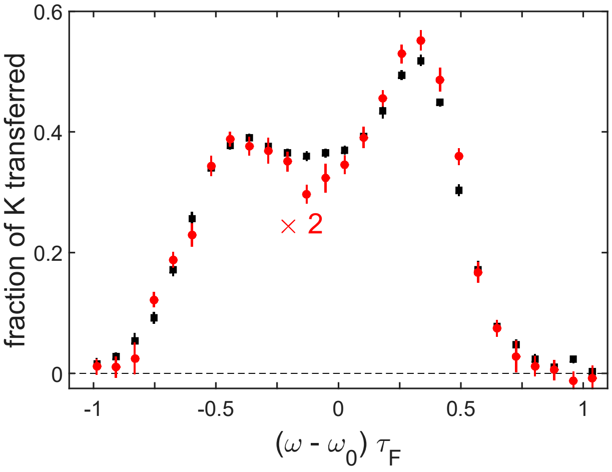

FIG. 14. **Linearity of the rf response for resonant interactions**. Fraction of the K atoms transferred from state K$|2\rangle$ to the state K$|3\rangle$ by an rf pulse with duration $t_{\rm rf} = 100\,\mu$s for $X = +0.02(6)$. For the black data points, the intensity of the rf pulse is adjusted to obtain a π-pulse in the absence of Li atoms. The red data points correspond to a 50% lower intensity of the rf field.

We checked the linearity of the response by varying the intensity $I_{\rm rf}$ of the applied rf field. Fig. 13A shows the fraction of the K atoms transferred from the K$|2\rangle$ to the K$|3\rangle$ state in the repulsive polaron regime, under conditions similar to those in the measurements shown in Fig. 3A. The frequency of the rf pulse is adjusted so that $(\omega_{\rm rf} - \omega_0)\tau_F = 0.3$, corresponding to peak response and resonant excitation of the repulsive polaron. The rf intensity is measured in units of the intensity I_π that results in a π-pulse for noninteracting K atoms. For intensities up to the intensity $I_{\rm rf} = 0.79\,I_\pi$, which is used in the measurements shown in Figs. 3A and 3B, we observe that the transferred fraction of the K atoms stays essentially proportional to the intensity of the pulse.

In the linear-response regime, the atomic response is predicted to be proportional to the duration of the rf pulse. Fig. 13B shows the fraction of the K atoms transferred in the repulsive polaron regime by rf pulses with $I_{\mathrm{rf}} = 0.79\ I_{\pi}$, as a function of the pulse duration. The frequency of the rf pulse is adjusted so that $(\omega_{\mathrm{rf}} - \omega_0)\tau_F = 0.3$, in order to obtain the peak response, as in Fig 13A. For pulses with duration up to 300 μs (indicated by the dashed line), we observe that the transferred fraction of the K atoms stays essentially proportional to the duration of the pulse.

Note that the maximal transferred fraction exceeds 0.5. We explain this observation by the coupling of the initial non-interacting K state to multiple interacting K states by the rf pulse, which manifest themselves as the polaron peak and the broad pedestal in our spectra.

The spectra for resonant Li-K interactions shown in Figs. 3B, 11A, 11B were recorded using Blackman-shaped rf pulses with duration of $t_{\mathrm{rf}} = 100\,\mu$s (approximately $35\,\tau_F$). The intensity of these pulses was adjusted to 50% of that needed to produce π pulses for noninteracting K atoms. We verified the linearity of the rf response by comparing the spectra recorded using this rf intensity to those recorded using the intensity needed to produce full π pulses for noninteracting K atoms (Fig. 14). Our observations are in good agreement with linear response.

---

[1] F. Krausz and M. Ivanov, Rev. Mod. Phys. **81**, 163 (2009).
[2] R. Pazourek, S. Nagele, and J. Burgdörfer, Rev. Mod. Phys. **87**, 765 (2015).
[3] A. D. Cronin, J. Schmiedmayer, and D. E. Pritchard, Rev. Mod. Phys. **81**, 1051 (2009).
[4] J. Simon, W. S. Bakr, R. Ma, M. E. Tai, P. M. Preiss, and M. Greiner, Nature (London) **472**, 307 (2011).
[5] M. Atala, M. Aidelsburger, J. T. Barreiro, D. Abanin, T. Kitagawa, E. Demmler, and I. Bloch, Nature Physics **9**, 795 (2013).
[6] M. Gring, M. Kuhnert, T. Langen, T. Kitagawa, B. Rauer, M. Schreitl, I. Mazets, D. A. Smith, E. Demler, and J. Schmiedmayer, Science **337**, 1318 (2012).
[7] Z. Hadzibabic, P. Krüger, M. Cheneau, B. Battelier, and J. Dalibard, Nature (London) **441**, 1118 (2006).
[8] M. Koschorreck, D. Pertot, E. Vogt, and M. Kohl, Nat. Phys. **9**, 405 (2013).
[9] A. B. Bardon, S. Beattie, C. Luciuk, W. Cairncross, D. Fine, N. S. Cheng, G. J. A. Edge, E. Taylor, S. Zhang, S. Trotzky, et al., Science **344**, 722 (2014).
[10] J. Goold, T. Fogarty, N. Lo Gullo, M. Paternostro, and T. Busch, Phys. Rev. A **85**, 063632 (2011).
[11] M. Knap, A. Shashi, Y. Nishida, A. Imambekov, D. A. Abanin, and E. Demler, Phys. Rev. X **2**, 041020 (2012).
[12] M. Cetina, M. Jag, R. S. Lous, J. T. M. Walraven, R. Grimm, R. S. Christensen, and G. M. Bruun, Phys. Rev. Lett. **115**, 135302 (2015).
[13] See supplementary materials.
[14] D. Naik, A. Trenkwalder, C. Kohstall, F. M. Spiegelhalder, M. Zaccanti, G. Hendl, F. Schreck, R. Grimm, T. Hanna, and P. Julienne, Eur. Phys. J. D **65**, 55 (2011).
[15] J. Loschmidt, Sitzungsberichte der Akademie der Wissenschaften, Wien **73**, 128 (1876).
[16] R. A. Jalabert and H. M. Pastawski, Advances in Solid State Physics **41**, 483 (2001).
[17] P. Massignan, M. Zaccanti, and G. M. Bruun, Rep. Prog. Phys. **77**, 034401 (2014).
[18] F. Chevy, Phys. Rev. A **74**, 063628 (2006).
[19] P. Nozières and C. T. de Dominicis, Phys. Rev. **178**, 1097 (1969).
[20] C. Kohstall, M. Zaccanti, M. Jag, A. Trenkwalder, P. Massignan, G. M. Bruun, F. Schreck, and R. Grimm, Nature (London) **485**, 615 (2012).
[21] J. Dubois, T. Jullien, F. Portier, P. Roche, A. Cavanna, Y. Jin, W. Wegscheider, P. Roulleau, and D. C. Glattli, Nature (London) **502**, 659 (2013).
[22] C. Mora and F. Chevy, Phys. Rev. Lett. **104**, 230402 (2010).
[23] Z. Yu, S. Zöllner, and C. J. Pethick, Phys. Rev. Lett. **105**, 188901 (2010).
[24] W. Zwerger, ed., *The BCS-BEC Crossover and the Unitary Fermi Gas* (Springer, Berlin, 2012).
[25] R. A. Hart, P. M. Duarte, T.-L. Yang, X. Liu, T. Paiva, E. Khatami, R. T. Scalettar, N. Trivedi, D. A. Huse, and R. G. Hulet, Nature (London) **519**, 211 (2015).
[26] L. J. LeBlanc and J. H. Thywissen, Phys. Rev. A **75**, 053612 (2007).
[27] C. Chin, R. Grimm, P. S. Julienne, and E. Tiesinga, Rev. Mod. Phys. **82**, 1225 (2010).
[28] R. Schmidt, S. Rath, and W. Zwerger, Eur. Phys. J. B **85**, 1 (2012).
[29] G. M. Bruun and C. J. Pethick, Phys. Rev. Lett. **92**, 140404 (2004).
[30] D. S. Petrov, Phys. Rev. Lett. **93**, 143201 (2004).
[31] K. Góral, T. Köhler, S. A. Gardiner, E. Tiesinga, and P. S. Julienne, J. Phys. B **37**, 3457 (2004).
[32] M. H. Szymańska, K. Góral, T. Köhler, and K. Burnett, Phys. Rev. A **72**, 013610 (2005).
[33] M. M. Parish and J. Levinsen, Phys. Rev. A **87**, 033616 (2013).
[34] J. Vlietinck, J. Ryckebusch, and K. Van Houcke, Phys. Rev. B **87**, 115133 (2013).
[35] L. S. Levitov, H. Lee, and G. B. Lesovik, J. Math. Phys. **37**, 4845 (1996).
[36] L. Levitov and G. Lesovik, JETP Lett. **58**, 230 (1993).
[37] I. Klich (Kluwer, Dordrecht, 2003), pp. 397–402.

[38] A. Rosch, Adv. Phys. **48**, 295 (1999).
[39] P. W. Anderson, Phys. Rev. Lett. **18**, 1049 (1967).
[40] R. Combescot and S. Giraud, Phys. Rev. Lett. **101**, 050404 (2008).
[41] G. D. Mahan, *Many-particle physics*, Physics of solids and liquids (Plenum, New York, NY, 1990).
[42] K. Ohtaka and Y. Tanabe, Rev. Mod. Phys. **62**, 929 (1990).
[43] J. Korringa, Physica **16**, 601 (1950).
[44] G. Yuval and P. Anderson, Phys. Rev. B **1**, 1522 (1970).
[45] A. Trenkwalder, C. Kohstall, M. Zaccanti, D. Naik, A. I. Sidorov, F. Schreck, and R. Grimm, Phys. Rev. Lett. **106**, 115304 (2011).
[46] F. M. Spiegelhalder, A. Trenkwalder, D. Naik, G. Kerner, E. Wille, G. Hendl, F. Schreck, and R. Grimm, Phys. Rev. A **81**, 043637 (2010).
[47] M. Kasevich and S. Chu, Phys. Rev. Lett. **69**, 1741 (1992).